2022

Design of a Surrogate Hypersonic Inlet for the HIFIRE-6 Configuration

Joseph W. Mileski
Wright State University

DESIGN OF A SURROGATE HYPERSONIC INLET FOR THE HIFIRE-6 CONFIGURATION

A Thesis submitted in partial fulfillment of the
requirements for the degree of
Master of Science in Mechanical Engineering

by

JOSEPH W. MILESKI

B.S., Ohio Northern University, 2012

B.S.M.E., Ohio Northern University, 2020

2022

Wright State University

Disclaimer

The views expressed are those of the authors and do not reflect the official guidance or position of the United States Government, the Department of Defense, the United States Air Force, or the United States Space Force.

WRIGHT STATE UNIVERSITY

GRADUATE SCHOOL

July 22, 2022

I HEREBY RECOMMEND THAT THE THESIS PREPARED UNDER MY SUPERVISION BY Joseph W Mileski ENTITLED Design of a Surrogate Hypersonic Inlet for the HIFiRE-6 Configuration BE ACCEPTED IN PARTIAL FULFILLMENT OF THE REQUIREMENTS FOR THE DEGREE OF Master of Science in Mechanical Engineering.

_____

Mitch Wolff, Ph.D.
Thesis Director

_____

Raghavan Srinivasan, Ph.D.
P.E.
Chair, Department of
Mechanical and Materials
Engineering

Committee on Final Examination:

_____

Mitch Wolff, Ph.D.

_____

Mark A. Hagenmaier, Ph.D.

_____

José A. Camberos, Ph.D. P.E.

_____

Barry Milligan, Ph.D.
Dean of Graduate School

ABSTRACT

Mileski, Joseph W. M.S.M.E., Wright State University, Department of Mechanical and Materials Engineering 2022. Design of a Surrogate Hypersonic Inlet for the HIFIRE-6 Configuration

Shock wave-boundary layer interactions can significantly impact the operability of high-speed inlets by inducing flow separation. This flow separation is difficult to visualize in three-dimensional, inward-turning inlets because of the curved surfaces that form their internal flow paths. To remedy this challenge, a surrogate test article was created. Using the results from a previously completed Computational Fluid Dynamic (CFD) analysis of the HIFiRE-6, a surrogate inlet with a rectangular isolator section was streamline-traced, allowing for the use of schlieren imagery to capture the separation bubble. This thesis discusses the process of developing the test article. Experimental results from a planned future test entry will be compared to CFD results and wind tunnel results from previous tests, to examine the suitability of this surrogate.

TABLE OF CONTENTS

List of Figures

List of Tables

Glossary of Symbols

u_r .....radial component of velocity

u_θ .....angular component of velocity

θ .....angle

u' .....derivative of velocity with respect to angle

r .....radial distance

δ_1.....Displacement thickness

γ .....Ratio of specific heats

M_∞.....Freestream Mach number

Re_{x_∞} .....Freestream unit Reynolds Number

v .....velocity

U_∞ .....Freestream velocity

Re_x .....Unit Reynolds number

M .....Mach Number

Re .....Reynolds number

p_{0_∞} .....freestream total pressure

p_e.....total pressure at the edge of the boundary layer

ρ_w .....density of air at the wall

μ_w .....viscosity of air at the wall

ρ_e.....density of air at the edge of the boundary layer

μ_e.....viscosity of air at the edge of the boundary layer

F_N .....Normal Force

F_A .....Axial Force

p .....Static pressure

T_s.....Tensile Strength

E.....Modulus of Elasticity

A_t.....Tensile-Stress Area

l_d.....Thread lengthk_b Bolt Stiffness

k_m.....Member Stiffness

S_p.....Proof Strength

F_i.....Preload

η.....Safety Factor

F'.....Direct Shear

F''.....Moment Shear

σ.....stress

t.....thickness

d.....diameter

Dedication

This thesis is dedicated to all students who start a new career path. Though the road may be hard, and you may grow tired, it is always worth it. To pick yourself up after defeat, deciding that a new path must be cut will lead to great things. Through this project I have been in that space, and here I am at the end seeing all that has gotten me here and can only think “It was rough getting here but look at where I have come”. You too can find your mountain top and look back at the hills and valleys that got you there. Hike on!

Acknowledgements

The author would like to thank those that have been influential in the completion of this thesis project. To his advisor Dr. Mitch Wolff, deep gratitude for the opportunity to walk into such a rich project and always believing in the ability to continue. To the team of Heidi Wilkin and Tyler Gardner, your faith that the project would be a success and your ever present reminds that the work was good enough. To Lois Weir, your experience in inlet design and testing, as well as your well-spring of references cannot be expressed. You have been the greatest of helps and a great role model, illustrating what a successful career in this industry looks like. To Dr. Jose Camberos and Dr. Craig Baudendistel, your expertise in fields outside the scope of this project has been invaluable in completing it. To the employees of Open Additive, especially Dr. Chris Barrett, your acceptance of my constant presence in your office, attempting a build unlike anything else you have done and endless knowledge on additive manufacturing was greatly appreciated. And finally, to my family, without your support I would never have completed another degree. Your love and support has been my crutch to climb this seemingly endless hill.

This thesis was completed with funding from the Air Force Research Laboratory (AFRL) and the Defense Associated Graduate Student Innovators (DAGSI).

I. BACKGROUND REVIEW

1.1 High speed propulsion

The design of high-speed vehicles has been a continued topic of interest in the aerospace community. Several types of engines have been suggested as means to continue to accelerate to higher speeds, Figure 1.

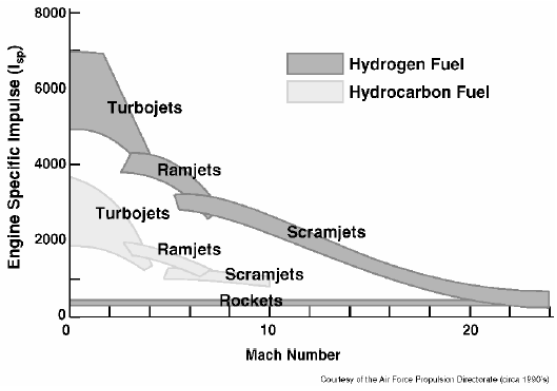

Figure 1: Graph of various engines type specific impulse with respect to Mach number [1].

As shown in Figure 1, rockets function at all speeds, but are inefficient largely because they must carry oxidizer onboard in addition to fuel. Turbojets are much more efficient, but only at lower speeds. At speeds above Mach 3, machinery is no longer needed to compress the air entering the combustor [2]. Without these mechanical components, the ramjet makes it possible to increase the temperature, continuing to allow higher speeds.

1.1.1 Ramjet

René Lorin developed the concept of the ramjet in 1913 [2]. The ramjet does not use any fan or other machinery to compress the air, but rather uses changes in the geometry to compress the air using a series of shock waves. These shocks are created using the geometry of the forebody turning toward the throat, ending in a normal shock on or near the throat [3], as shown in Figure 2.

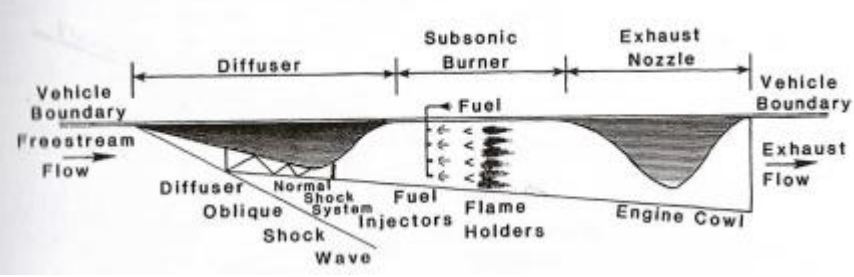

Figure 2: Diagram of ramjet engine [3].

The normal shock acting within the throat of a ramjet causes the air within the engine to drop from supersonic to subsonic, producing flow velocity that is compatible with the ignition source[4]. However, due to the nature of a normal shock [5] at higher flight speeds, considerable pressure loss occurs due to this transition from supersonic to subsonic flow velocities [2]. To avoid this pressure loss, the compression section must consider supersonic flowthrough.

1.1.2 Scramjet

A scramjet, or supersonic compression ramjet, is the response to the need of maintaining supersonic flow thru. By removing the normal shock at the throat, and introducing an internal oblique shock train, Figure 3, the flow through the isolator stays at supersonic speeds, increasing the pressure throughout the engine.

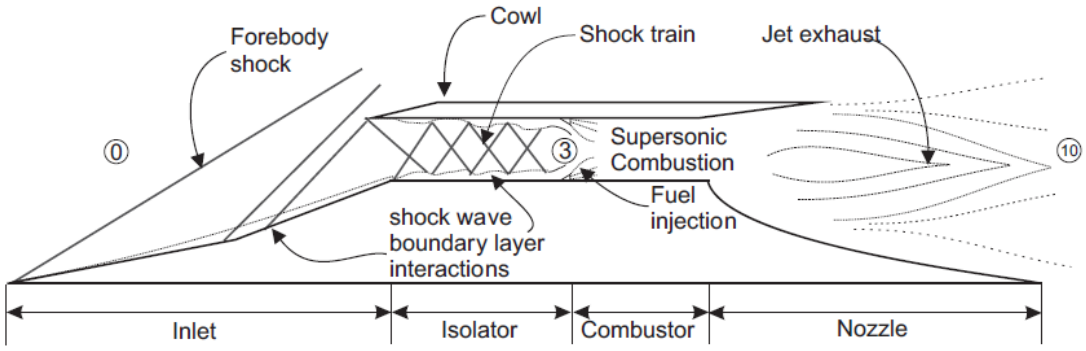

Figure 3: Diagram of a scramjet engine [6].

Weber and MacKay show that the efficiency of a scramjet surpasses that of a ramjet configuration at approximately Mach 5 [7]. Therefore, at speeds above this point, it is a better design choice to maintain supersonic flow throughout the engine flowpath.

Heiser and Pratt detail six common configurations for the compression system used in ram and scram engines [3]. They begin with external compression with a normal shock wave, where the shock wave is formed upstream of the cowl lip. This allows for spillage, or ejection of excess flow, and due to the normal shock, is ineffective at higher speeds. The next configuration is the external compression with an oblique shock. Using a series of ramps, the compression surface generates oblique shock waves that compress the air entering the engine. Having these shock waves focus on the cowl lip, the flow downstream of the final shock is parallel and uniform, which is desirable for efficient

combustion. The next configuration is very similar to the last, as it is an external compression formed by oblique shocks, however, the compression is isentropic. This is accomplished by having a continuously turning surface. They continue with the mixed compression system. This uses the external oblique shock compression, but instead of the shocks cancelling at the cowl lip, it also has internal shock waves which continue compression after the cowl lip. This allows the compression system to include an isolator section that compresses internally using weaker shocks with smaller entropy increases than purely external compression. Another compression system mentioned is the lateral mixed compression, which uses a series of channels that allows a shorter length, but introduces interactions between the separate oblique shocks, making the flow field difficult to analyze. The final configuration is the symmetrical internal compression system. This system uses a symmetric surface that cause the oblique shocks to generate parallel and uniform flow, and shortens the overall length needed for the compression. An axisymmetric version of this is known as the Busemann inlet.

1.1.3 Busemann inlets

A Busemann inlet is an axisymmetric, inward-turning inlet that functions as a single duct whose area changes. This area change is selected such that it forms an isentropic compression system ending in a conical shock, Figure 4 [8]. With a Busemann inlet, it is assumed that the flow is inviscid, axisymmetric, and irrotational.

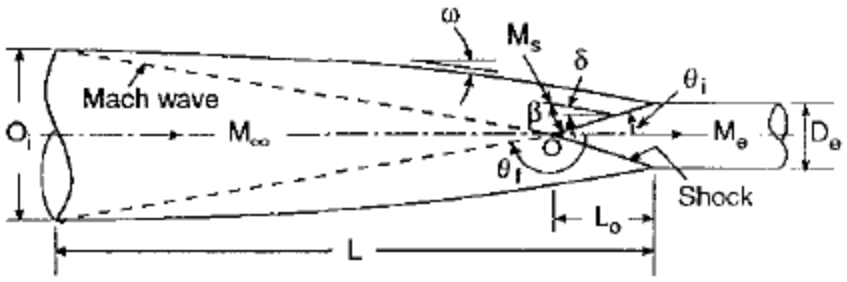

Figure 4: Diagram of a Busemann inlet [9].

The flow within Buesmann inlets can be modeled using the Taylor-Maccoll equation [10]. The Taylor-Maccoll equation for calorically perfect gas in a conical flow is:

$$u_R'^2(u_R + u_R'') = \frac{\gamma-1}{2}(1 - u_R^2 - u_R'^2)(u_R'' + u_R' + cot(\theta) + 2u_R) \quad (1)$$

where u_R is the velocity in the radial direction, u_θ is the velocity in the angular direction, θ is the angular location, and γ is the ratio of specific heats [11]. Figure 5 illustrates the different components of Equation 1.

$$u_\theta = u_R{}' \quad (2)$$

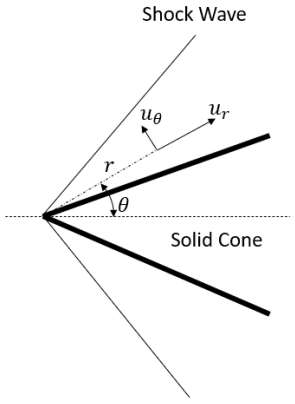

Figure 5: Model of supersonic flow passing over a cone, indicating the radial and angular position of a point, with respective velocities as demonstrated by Taylor and Maccoll [11].

We note that due to the assumption that the flow is irrotational,

Equation 1 is a second-order differential equation with respect to θ, so there must be two boundary conditions to evaluate a solution. The two conditions used are the flow upstream of the shock is parallel to the freestream and the Mach Number downstream of the shock, as well as the shock angle are known [10]. As the equation does not have a closed-form solution it must be solved iteratively [5].

One of the other assumptions for a true Busemann inlet is that the flow is inviscid, yet the reality of viscous effects must be considered. This is accomplished by identifying a displacement thickness in which the addition of space to account for the distance between the surface and freestream is added to the boundary [12]. A Busemann type design is ideal for hypersonic applications as it has low inviscid losses [13], though with drawbacks. Due to the nature of a symmetric compression system, operating off design produces complex flow patterns, or may even cause unstart. Flow separation is also common due to the strength of the conical shock [10], as well as the ideal Buesmann inlet is longer than other compression systems.

1.1.4 Self-Starting Busemann inlets

One of the most important characteristics of a functional high-speed inlet is that the inlet starts and remains started within the operability envelope. Unstart can occur when the flow within a mixed compression inlet contracts too much, leading to choking at the throat, or when the back pressure exceed the capability of the inlet [14]. An indication of unstart is that the shock at the cowl lip moves upstream of the cowl lip. To avoid unstart, it is common practice to ensure that the contraction ratio, the change in area from the leasing edge to the exit of the compression section, within the compression section of the

inlet remains between two limits. The lower limit is the isentropic limit, which is defined by the isentropic relation of area and Mach number of quasi-one-dimensional flow [5,14]. The upper limit is the Kantrowitz limit, which was defined by Kantrowitz while investigating the maximum contraction in supersonic diffusers [14,15]. Figure 6 shows the isentropic and Kantrowitz limits, as well as Van Wie's estimation of where ideal start occurs.

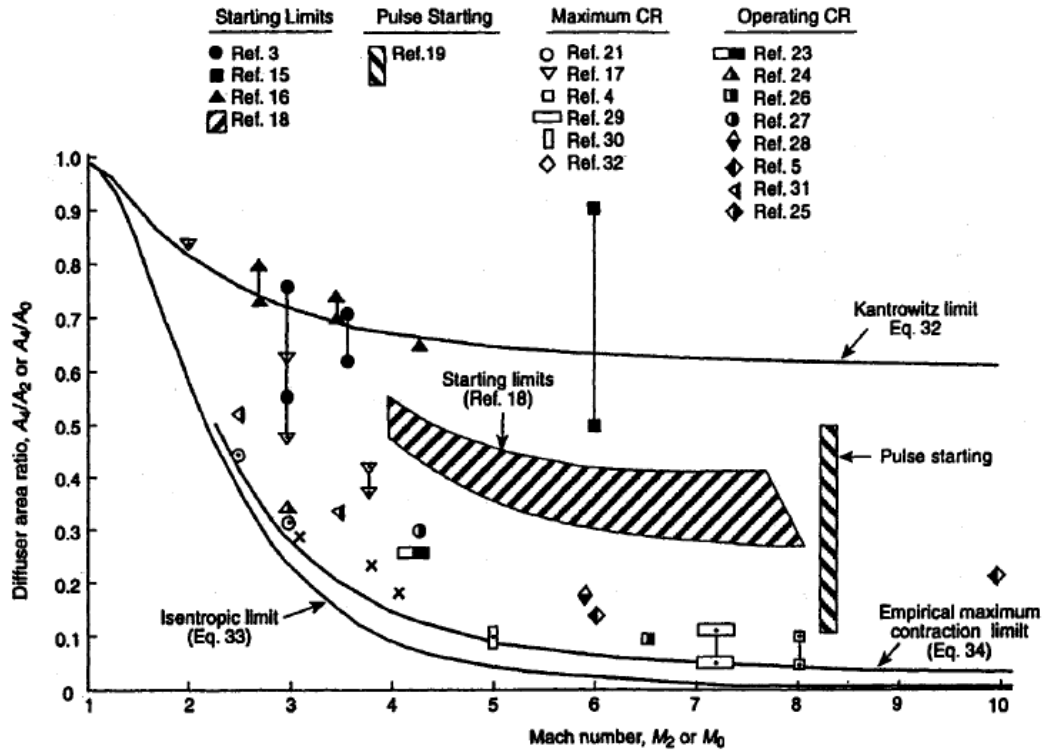

Figure 6: Diagram of starting limits determined by Van Wie [14].

It is important to be take into account starting limits as the viscous effects caused by the boundary layer may choke the flow especially in an inlet with strong compression and no bleed mechanisms to provide stability margin, such as a Busemann inlet [15]. A common solution to avoid such choke, is to allow flow spillage by truncating the cowl lip, the lower leading edge [16]. This essentially moves the cowl lip downstream of the leading edge, causing the inlet to no longer be completely axisymmetric.

1.1.5 HIFiRE-6

One such design of a Busemann style scramjet inlet with a translated cowl lip is the HIFiRE-6 202E Configuration, Figure 7.

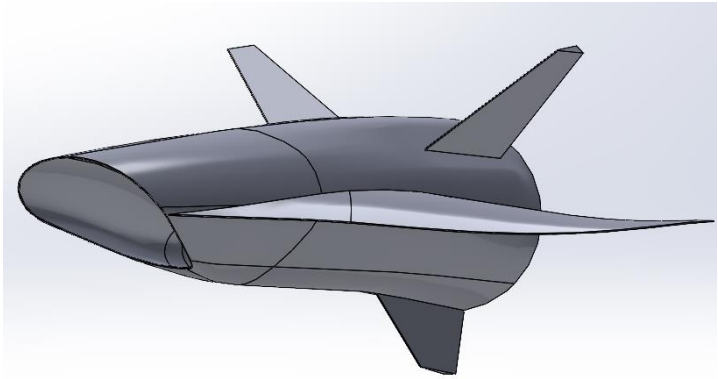

Figure 7: HIFiRE-6 202e Configuration. Showing the truncated Busemann style inlet.

The Hypersonic International Flight Research and Experimentation Program (HIFiRE) was conducted as a partnership between AFRL and the Defence Science Technology Organisation (DSTO) of Australia and focused on building understanding of hypersonic flow phenomena and technologies to improve the use of vehicles functioning in those conditions [17]. The purpose of the HIFiRE program is to help in maturing the technologies needed to develop the next generation of aerospace systems and validate the theory of those systems in conditions where ground testing and computational methods are lacking [18]. The program was intended to complete up to 10 different research projects. Each Project, designated by its flight number, would have a different focus, looking to characterize a fundamental hypersonic phenomenon and quantify its effects on the vehicle. Table 1 shows each flight and its primary objective.

Table 1: Each HIFiRE Flight with Primary Objective [19]*, showing the wide range of hypersonic phenomena investigated in the program.*

Flight	Primary Objective
1	Boundary Layer Transition
2	Dual-to-scram transition
3	Radical Farming scramjet combustion
4	Hypersonic waverider
5	Boundary layer transition with 3-D Effects
6	Adaptive Flight control
7	REST inlet
8	Airframe integration of HIFiRE-7

The HIFiRE-6 geometry was designed with a highly-integrated inward-turning inlet optimized for cruise conditions at Mach 6 and an equivalent dynamic pressure of 1000 psf [20]. Wind tunnel testing has been performed on the HIFiRE-6 collecting pressure data, schlieren imagery [17], and CFD data [21].

1.2 Shock Wave-Boundary Layer Interaction

The boundary layer at high Reynolds numbers thins due to the no slip boundary condition at the wall [22]. Because the boundary layer is thin, resolving a zero velocity at the surface, and a high speed flow at the edge of the surface, causing the boundary layer to separate from the wall. This occurs due to the creation of an adverse pressure gradient [23]. When shock waves within the compression system impinge on the boundary layer it may cause an area of recirculation, as shown in Figure 7, commonly referred to as a separation bubble [24]. This bubble can affect the compression process by restricting the area, potentially chocking the flow to the point of unstart.

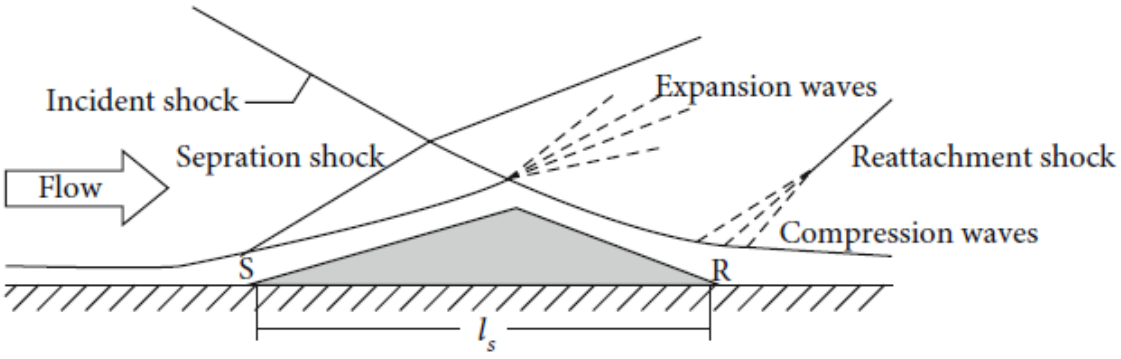

Figure 8: Schematics of boundary layer separation caused by the incident shock [25]. *The darker region shows the location of the bubble.*

The understanding of flow phenomena such as shock wave-boundary layer interaction is essential to gaining a higher understanding of how inlets work at these high speeds and how to better manage the unique flow physics of high-speed flights.

1.3 Modelling and Testing Methods

1.3.1 Streamline Tracing

Several methods exist to design the compression system of a scramjet inlet. The first and most fundamental is using the Method of Characteristics [26]. This process solves the characteristic equations and compatibility conditions, which define the nature of the flow at discrete points, moving in a positive and negative direction. Using either a surface boundary condition, where the turning angle is zero, or a free boundary using desired conditions at a specific point, the characteristic equations can be iteratively solved producing a flowfield.

Another method of design is the use of a series ramps to achieve the compression desired [27]. This method uses oblique shock relations to compress the air from the free stream conditions to the desired isolator entrance conditions. The compression section can also be designed using quasi 1-D flow. This process uses the assumptions 1) One-dimensional flow, where the boundary layer is represented by its average, 2) Air is a calorically perfect gas, and 3) Heat transfer to and from the wall can be neglected [28]. This method is a simplified version of the series of ramps, with ideal assumptions.

Streamline-tracing is another technique used in inlet design. In 1966, Mölder and Szpiro proposed the concept to develop a Busemann inlet that would remain self-started [10]. They suggested that after creating a flow field, streamlines could be created that would produce the geometry of the desired inlet. Using the desired compression ratio and Mach numbers for at least two stations, a flow field can be created or a parent flow field can be selected [29]. Next, the streamlines are generated within this flow field by defining a shape at the inlet exit and following them upstream until they are parallel to the freestream flow [30]. The streamlines can then be replaced with a solid surface to create the interior surface of the model [31]. This process produces an inviscid model, so it follows that viscous effects such as displacement thickness must be considered and corrected for the inlet to provide the desired Mach reduction. When a parent geometry is available, streamline tracing is the best option, as calculating the characteristics is redundant and a series of ramps cause unnecessary pressure loss.

1.3.2 Schlieren Imagery

To augment traditional data measurements (pressure and temperature), visual measurement data can be collected. Visual data is advantageous as it produces a more complete picture of the flow field while remaining non-intrusive, since it does not need instrumentation within the flowpath [32]. One method of visual measurement is schlieren imagery. Schlieren was developed by August Toeple in the 1800's. This process is different from shadowgraphy, which visualizes the density of a flow. Schlieren imagery visualizes a gradient, usually density, to note the changes in the media. This is where schlieren gets its name, as this leads to the term used in German for the optical inconsistency of glass [33].

Schlieren uses a series of lenses and mirrors to focus on the test section to determine the change in density of the working fluid within that test section by measuring the density gradient at two consecutive times [34]. Using a high-speed camera and high-powered light source, such as a laser, the images are able to capture quickly changing phenomena such as turbulent structures. There are several different types of schlieren, though traditional gray scale is preferred for high speed applications, as problems with glass and vibration from the tunnel are able to be mitigated [35].

II. INTRODUCTION

Increased understanding of the flow physics that govern high speed compression system operability and performance can lead to improvements such as shorter inlet/isolator designs. This can lead to a decrease in overall vehicle length and weight. To make these adjustments, the flow phenomena within the interior flow path (IFP) needs to be investigated. While it is relatively simple to instrument the IFP of a wind tunnel test article to obtain static and dynamic pressure measurements, these measurements only provide information at discrete locations (usually surface measurements). To investigate the IFP more thoroughly, a visual measurement technique - such as schlieren imagery or Pressure Sensitive Paint (PSP), is often used to supplement the information provided by pressure taps. The geometry investigated can affect the ease at which capability to record flow visualization data can be easily accomplished. For two-dimensional geometries is it fairly simple, but three-dimensional geometries it can be challenging to incorporate the ability to visualize the internal flow path into the wind tunnel test article. The geometry of an inward-turning scramjet inlet such as the HIFiRE-6 involves curved surfaces and circular ducts that make it difficult to incorporate windows or transparent sections for flow visualization. Therefore, a surrogate was developed that is intended to mimic the flow physics of the HIFiRE-6 inlet while providing an isolator with a rectangular cross-section. Using the results from a Computational Fluid Dynamics (CFD) analysis of the HIFiRE-6, streamline-tracing was used to design a surrogate model with a rectangular

isolator section. The HIFiRE-6 inlet configuration was selected as the parent for this surrogate for two main reasons. First, the HIFiRE-6 contains a 3D compression system that creates a complex flow field with flow phenomena of interest, such as a separation bubble. Second, models of the HIFiRE-6 have been previously tested in various wind tunnels, providing both experimental and CFD results [17]. These data sets will be used as a comparison to assess the viability of the model described as a surrogate for the HIFiRE-6.

The model designed for this thesis will be tested to investigate the Shock Wave – Boundary Layer Interaction (SWBLI) induced by the cowl shock on the windward (body-side) surface of the IFP. Special emphasis is placed on the separation bubble caused by this SWBLI because it has a large impact on the operability of the inlet. Using a combination of pressure measurements and schlieren imagery the location and extent of the separation bubble will be determined as it changes with Reynolds number and angle of attack. The suitability of the model to serve as a surrogate for the HIFiRE-6 inlet, mimicing its shock structure and compression, will be evaluated to assess feasibility for future high speed flow research.

The following sections detail the methodology used for the aerodynamic design and fabrication of the surrogate model, including streamline tracing, mesh generation, boundary layer corrections, and CAD model development. A brief section on the additive manufacturing process used to fabricate the model is then covered. This thesis concludes with key outcomes and lessons learned.

III. EXPERIMENTAL DESIGN

The design process for the surrogate test article evolved with the general objective to produce a surrogate test article to simulate the HIFiRE-6 flow field. In its final iteration, the design process included generating streamlines from CFD results, adjusting the stream traces, creating surfaces from the streamlines, and adding instrumentation. This chapter will describe in more detail.

3.1 2-D Geometry Generation

To meet the objective of performing schlieren flow visualization, the geometry of the model required a unique approach. It was determined that a two-dimensional model would be ideal to best visualize the flow physics within the compression and isolator sections. The SUPIN design tool [36] was used to develop an initial fully two-dimensional inlet configuration.

SUPIN is a single solver program that uses an input file to generate a geometry that meets the characteristics dictated by the input file. The input file uses the form shown in Appendix A, regarding what characteristics can be used. The characteristics specified from the HIFiRE-6 are shown in Table 2. Emphasis is placed on freestream Mach number, Reynolds number, total temperature, and total pressure.

Table 2: Conditions used for the SUPIN input file, constructed for previous testing on the HIFiRE-6 utilized in previous testing.

Gas Properties			
Specific gas constant	=	1716.49	ft lbf/(slug R)
Ratio of specific heats	=	1.4	
Sutherland's Constants			
Reference viscosity	=	3.62E-07	slug/ft-s
Reference temperatur	=	518.7	R
Constant	=	198.72	R
Flight Conditions			
Altitude	=	90000	ft
Mach	=	6	
Temperature	=	403.13	R
Pressure	=	0.255	psi
Viscosity (Sutherland)	=	2.96E-07	slug/ft-s
Density	=	5.31E-05	slug/ft^3
Speed of sound	=	984.25	ft/s
Reference length	=	7.5	ft
Re/ft	=	1.06E+06	1/ft
Reynolds number	=	7.95E+06	

These conditions were used to create the input file, Appendix B. Using this input file SUPIN generated a geometry using method of characteristics for the compression and isolator sections, Figure 9.

Figure 9: SUPIN generated 2-D geometry that mimics HIFiRE-6 characteristics.

Throughout the process of using SUPIN, adjustments have been made to reflect the shock instead of cancelling it with a terminal normal shock allowing for supersonic

flow throughout the internal flowpath. However, the process of creating a shock train within the isolator section has not been completed. As shown in Figure 10, the method of characteristics for different stations within the compression section was able to be generated, showing what the flow field should be within the flowpath.

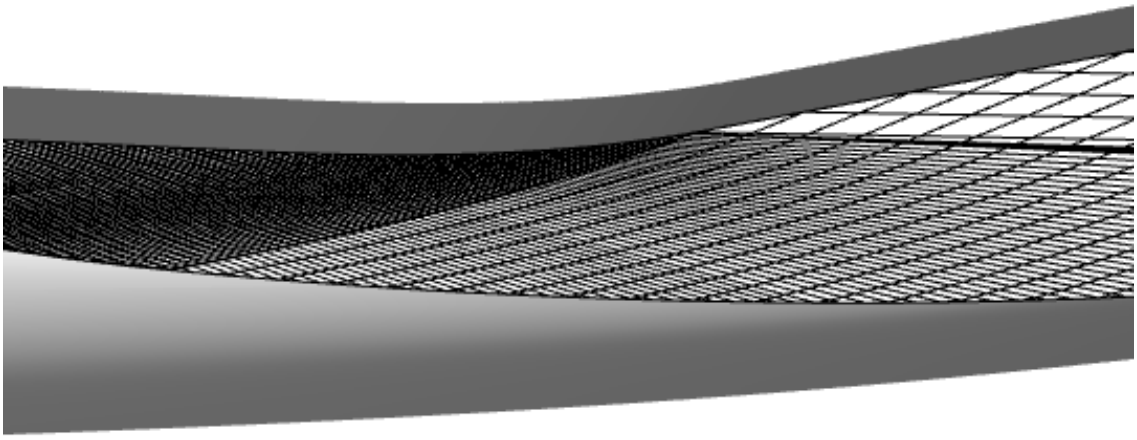

Figure 10: SUPIN generated geometry with MOC grids showing reflected cowl shock where grids meet.

Due to the limitations of the SUPIN tool, it was difficult to design a configuration with an internal reflecting shock that would adequately mimic the SWBLI of interest in the HIFiRE-6 configuration. It was also found that the overall dimensions of a fully 2D inlet model (with a sufficiently tall isolator) would exceed the maximum allowed dimensions of the reference test facility, while also having an isolator entrance large enough to gather useful visual data. It was determined that a 3D inlet similar to that of the HIFiRE-6, but with a rectangular isolator section, would be the next best option.

3.2 Creating Streamline Traces

To generate an inlet with a rectangular isolator that would more closely mimic the unique compression system of the HIFiRE-6, streamline tracing [37] was used. Guided by the results of inviscid and viscous CFD analyses of the HiFiRE-6 Configuration 202E by Bisek [21] as the parent flow field, a CFD visualization and analysis tool, Tecplot®, was used to generate streamlines. This process started with examining a vertical slice along the centerline of the viscous analysis, shown in Figure 11, to determine the location of the separation bubble of interest to this investigation.

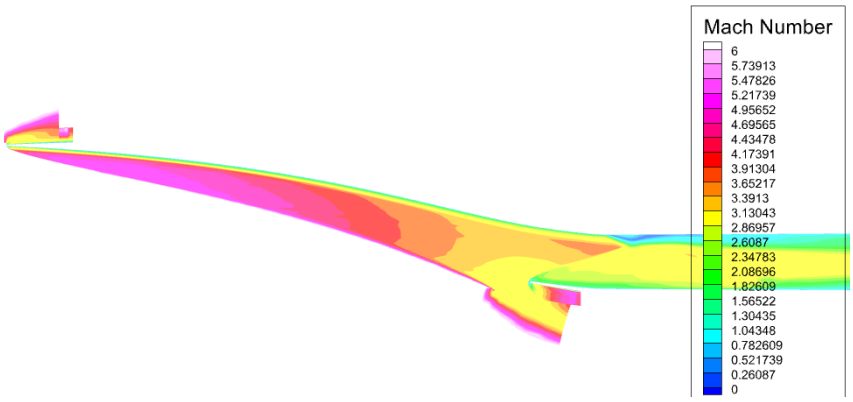

Figure 11: Viscous CFD results of the HIFiRE-6 along the centerline of the inlet, were used to determine the location of the separation bubble and select the axial location to seed streamlines.

A plane at a station near the separation bubble and normal to the *x*-axis (flow direction) was selected for the origin of the initial streamline-traces. On this plane, a region was then selected as a rectangle indicates where the isolator entrance would be within the flow field. Figure 12 shows the rectangle selected.

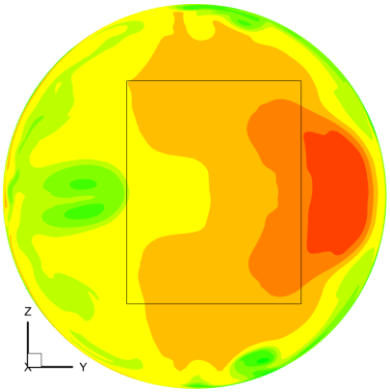

Figure 12: Cross-section of inviscid CFD results of HIFiRE-6 used to locate the rectangle on which streamline seeds were placed.

Using this rectangle imposed on the inviscid results at the same location in the flowfield, eleven equally spaced streamline seeds were placed on each edge of the rectangle as shown in Figure 13. The upstream-flowing streamlines were then exported individually as text files, which were then imported as an array into MATLAB®.

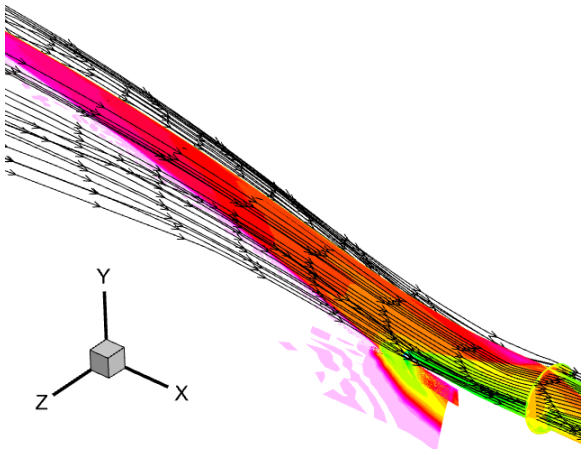

Figure 13: CFD results of the HIFiRE-6 with streamlines placed just upstream of the separation bubble. This axial location of the cross section and rectangle produced the best streamlines of the evaluated options.

Planes at several locations, and rectangles of varying geometries were investigated to define the origin of the streamline seeds for development of the streamlined inlet geometry. The process described above was used to create, modify for viscosity, and define a surface in SOLIDWORKS® to identify any geometry issues. Many isolator rectangle locations and geometries that were investigated introduced one or more of three major issues. (1) When the streamwise location was too far upstream, the streamlines completely bypassed the separation bubble. (2) When the body-side edge of the rectangle was too high, the corners would interact with the surface causing abrupt direction changes. When placed too low, vorticity would cause the streamlines to intertwine. (3) When the cowl-side edge was too low, streamlines would move into the surface. When placed too high, it would cause the center to droop. Shifting the location of the seed plane in the streamwise direction would affect where these areas of concern would be located. After several iterations, the location of the rectangular seed isolator was placed just downstream from where the incident shock reflected on the shoulder of the inlet, see Figure 11 and Figure 12. This produced the cleanest streamlines that included a portion of the flow in the region where the separation bubble occurred in the viscous solution. Figure 11 shows the location of the rectangle relative to the cross-section, where Figure 12 illustrates the axial location of the cross-section relative to the whole flow-field. After the streamlines were generated, they were imported into MATLAB® to remove points downstream of the isolator entrance, upstream of the leading edge, and to be corrected for viscous effects.

3.3 Using MATLAB to Adjust Streamlines

MATLAB® was used to iteratively modify the stream traces derived from the original 3-D HIFiRE-6 flow field. For each configuration of streamlines, 44 text files containing the points of each streamline were imported into MATLAB®, and processed through a script. This script performed several functions and generated a new set of text files for troubleshooting purposes. The script started by addressing the first hurdle encountered in exporting streamlines from Tecplot®. Importing Tecplot® generated streamlines directly into the 3-D solid modeling software, SOLIDWORKS®, resulted in points that were identical or too close together to properly model. To correct this issue, the script used the 'uniquetol' function, which removed non-unique points within the array within a set tolerance. The tolerance selected was 5/10000". The streamlines were then trimmed to remove points downstream of the seed rectangle at the isolator entrance.

The streamlines were also trimmed to exclude points upstream of any turning in the parent flow field (points located in the freestream flow). This was accomplished by first adjusting for the angle of attack in the CFD analysis which was a positive four degrees. After the streamlines were rotated by the opposite angle (negative four degrees), the freestream was parallel to the horizontal axis. Taking the most upstream point of each streamline, a freestream *y* (up and down) and *z* (side to side) value was identified. Then each stream trace was trimmed upstream of the onset of turning by locating where the *y* or *z* coordinate first changed from the freestream value for that streamline, using that point as the leading point. Figure 14 shows an isometric view of the trimmed streamlines.

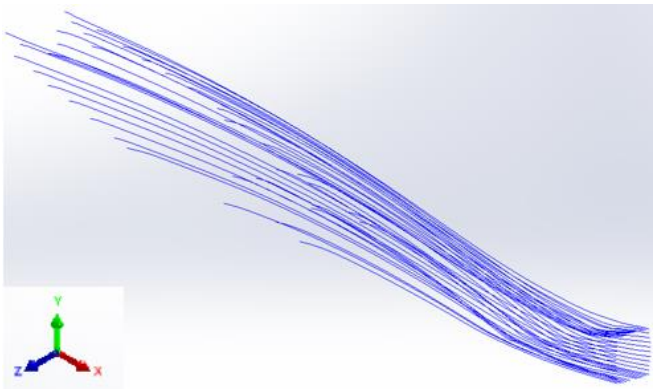

Figure 14: Isometric view of the trimmed streamlines. Extraneous points on the streamlines not used to generate the interior surface of the model inlet have been removed.

Once the streamlines were trimmed, a series of 1000 points were then extracted from each streamline at discrete, evenly spaced axial locations. Linear interpolation was used as necessary to determine each point. These evenly spaced points were used to create rings that connected the streamlines, as shown in Figure 15, by using similar indices of these points from all streamlines. The centroid of each ring was located and were collected and labeled as the ‘center curve’, which will be used in the next section.

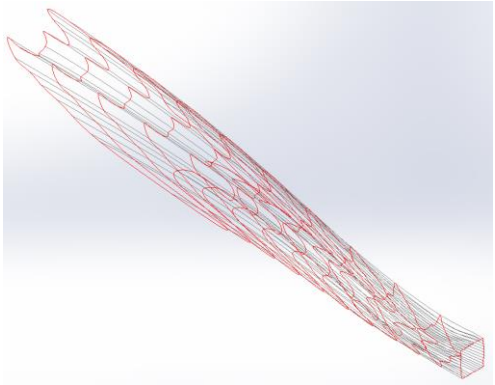

Figure 15: Isometric view of the streamlines (grey) with select rings (red).The centroid of the rings were used to create a center curve.

3.4 Boundary Layer Correction

Because an inviscid CFD solution was used to generate the streamlines, a viscous adjustment was applied to each streamline to adjust for boundary layer growth along the physical surface of the surrogate. In essence, an area relief was applied to "open" the streamlines downstream of the leading edge. This was accomplished by translating the streamlines out from the previously-defined center curve. To treat the center curve as a horizontal axis, each point on each streamline's y- and z-coordinates subtracted the closest upstream value of the center curve. Points upstream of the leading point of the center curve used the leading point, similarly points downstream of the trailing point used the trailing point. This translation allowed the points on each streamline to be transformed into cylindrical coordinates. Figure 16 shows the center curve (green line on the lower curves) as well as the adjusted curves (upper curves).

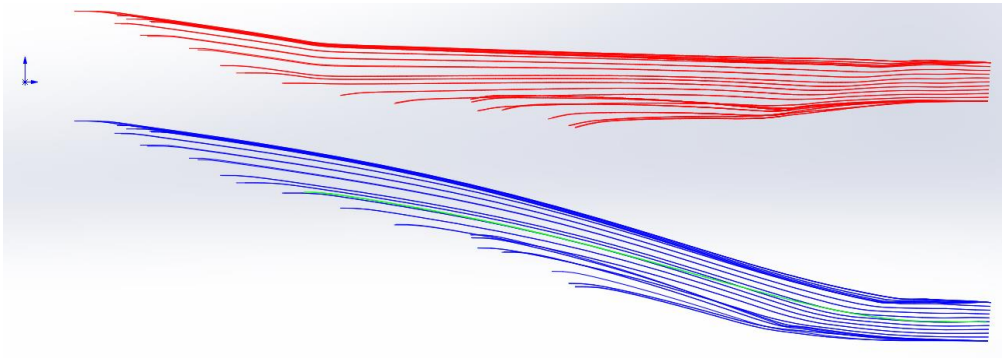

Figure 16: (Bottom) Trimmed streamlines with green center curve. (Top) Streamlines translated to align the center curve with the horizontal axis to transform into cylindrical coordinates. This transformation simplifies adjusting for boundary layer growth.

The radial component of each coordinate was adjusted outward by the estimated boundary layer displacement thickness at that location. Many different methods have been used for estimating boundary layer displacement thickness in hypersonic flows. Schlichting [12] defines displacement thickness as:

$$\frac{\delta_1(x)}{x} = \frac{\gamma-1}{\sqrt{2(2n-1)}} \frac{M_\infty^2}{\sqrt{Re_{x\infty}}} \sqrt{\frac{\frac{CR_\infty}{p_e}}{p_\infty}}\, I_1\left(\beta, \frac{T_w}{T_0}\right) \tag{3}$$

where the last two expressions, the radical and I_1, are assumed to be one and $n = 1.5$. For a flat plate, assuming an inward turning surface can be simplified as a series of flat plates, Schlichting defines the displacement thickness as:

$$\delta_1 = 1.7208\sqrt{\frac{\nu x}{U_\infty}} \quad . \tag{4}$$

Anderson [38] defines the displacement thickness with a cold wall as:

$$\delta_1(x) = \frac{1}{3}\left(\frac{C}{\sqrt{Re_x}}\, x^{\frac{3}{2}}\right), \tag{5}$$

where *C* is a similarity parameter assumed to be six, which was evaluated using other proportionalities, and including $\sqrt{x}$ in the denominator. Anderson also states that the displacement thickness is generally a third of the boundary layer thickness, introducing the $1/3$ to the equation. When not assuming a cold wall, Anderson presents the displacement proportion of:

$$\delta_1 \propto \frac{x}{\sqrt{Re}} M_\infty^2 \sqrt{\frac{Cp_\infty}{p_e}}, \;\; | \; C = \frac{\rho_w \mu_w}{\rho_e \mu_e}, \tag{6}$$

where the radical at the end is assumed to be one, and the proportionality constant, *C*, is assumed to be 0.04.

A comparison of the four expressions for displacement thickness is shown in Figure 17, Anderson's Cold Wall and Schlichting's Hypersonic expressions were identified as the best options, as they are more conservative. For this project displacement thickness was estimated by taking the average of these two expressions to incorporate some surface temperature effects.

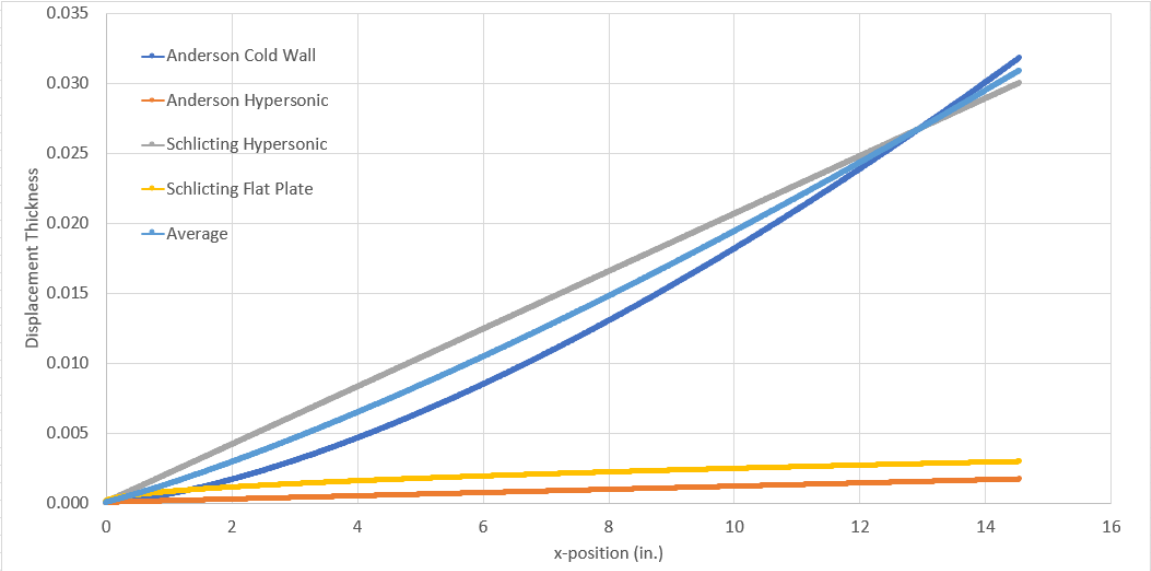

Figure 17: Comparison of displacement thickness expressions using the length of the non-dimensionalized streamlines assuming a cold wall

Using the distance along the streamline as the x-value in the displacement thickness calculation, the radial component of each point in the streamline was adjusted by the calculated displacement thickness. The streamlines were then transformed back from cylindrical coordinates to Cartesian, translated back from the centerline using the original distance, and rotated back by the angle of attack used in the CFD results. This produced stream traces corrected for viscous effects.

Because the streamlines were adjusted for boundary layer growth, the rectangle (used for seeding the streamlines) at the isolator entrance was no longer rectangular. Therefore, further adjustments of the streamlines was required to once again provide a fully rectangular entrance to the isolator section. At the location of the separation bubble, as predicted by the CFD results (the plane on which the original seed rectangle was created), a modified rectangle was generated by averaging the *y*-coordinates for the body and cowl side edges, and the *z*-coordinates for the side edges of the boundary-layer-adjusted streamlines. This produced four lines perpendicular to the flow that were used as the adjusted isolator entrance.

Because each streamline was a different length, the displacement thickness adjustment was applied differently to each line. This meant that the rectangle produced at the entrance of the isolator led to undesirable turning, Figure 18. To account for this, a weighted linear interpolation was used to force a smooth transition from the streamlines to the rectangle at the isolator. This weighted interpolation used a full interpolation at the isolator and left the leading edge unchanged. These averaged streamlines were then used to create ten new rings that were used to generate the interior surface of the model.

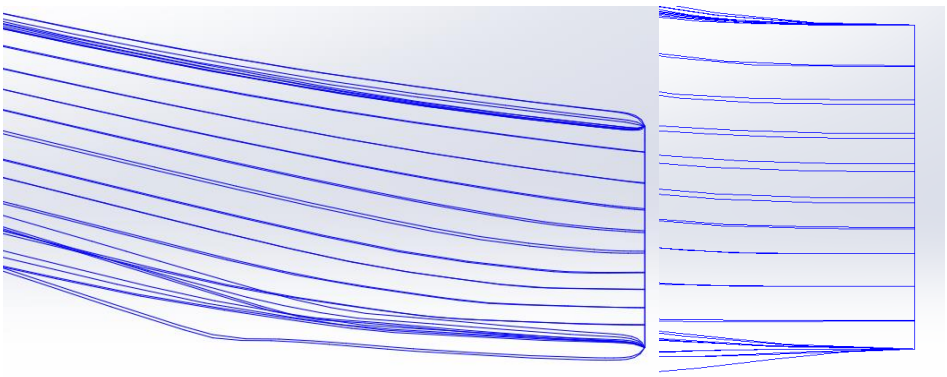

Figure 18: (Left) Isolator entrance after viscous correction, before weighted interpolation. (Right) Isolator entrance after viscous correction and weighted interpolation. With the interpolation, the 'approach' to the isolator does not have additional turning, which could affect the flow field.

3.5 Solid Model

After selecting the ideal streamlines and applying the previously described adjustments using the MATLAB® script, the streamlines and rings were imported into SOLIDWORKS® to generate the interior surface. Initially the interior surface was to be generated by creating surfaces between the generated rings. However, Figure 19 shows, the highlight of the inlet was concerning due to asymmetry, small channels, and a reduced capture area.

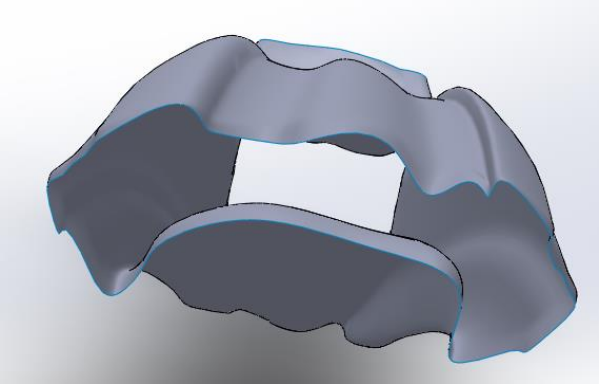

Figure 19: Initial highlight of generated streamlines. Note asymmetry and tight corners, which affect the resulting flow field.

Using adjacent streamlines, a reference surface was generated to observe where the rings intersected the streamlines. These areas were used to smooth out the rings, while maintaining the capture area at that plane. Figure 20 shows an area where this intersection was taking to illustrate the method used.

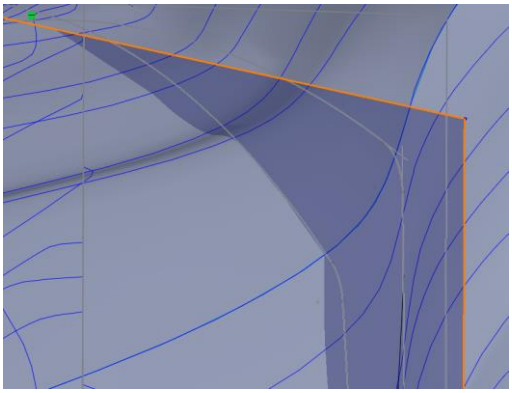

Figure 20: Illustration of planes used to generate the smoothed ring curves, showing how capture area was preserved. The blue rectangle shows the sketch plane used to assess the outline of each ring. The grey areas are the jagged surface.

This process was used to create smooth rings, shown in Figure 21. This removed all of the jagged edges, as well as the rising cowl lip. It was decided that, due to the streamlines passing through the center of the isolator section of the parent geometry, the rising cowl

lip would not allow enough spillage to avoid unstart so the rising section of the cowl lip was removed.

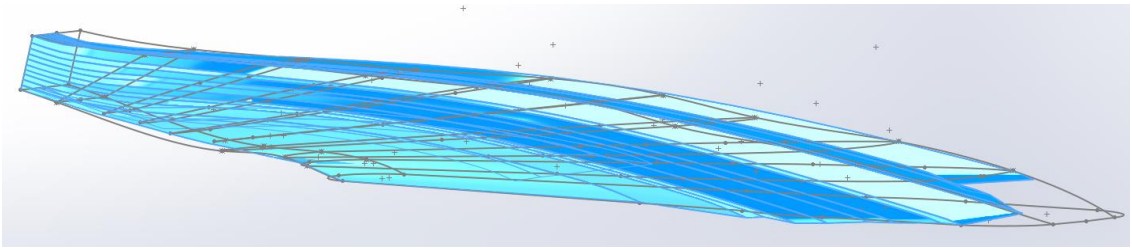

Figure 21: Streamline generated surfaces (blue) with smoothed ring curves (grey)

It was observed that due to the stream traces at the corners of the rectangle used, there were streamlines that extended further upstream, Figure 22. This caused the highlight of the inlet to have extreme curves, which was undesirable. To adjust for these issues, the most upstream ring, shown in red, was neglected. This removal was considered to be equivalent to a standard Busemann truncation [8].

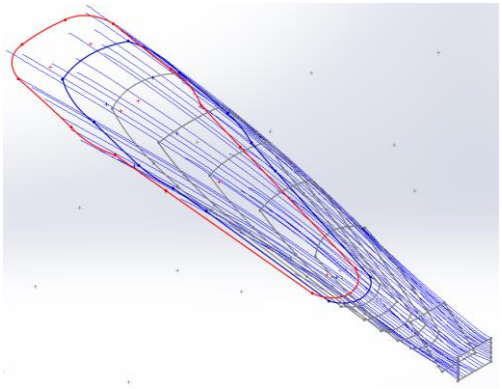

Figure 22: Isometric view of smoothed rings. These rings were used to generate a lofted surface. The leading ring (red) was removed to adjust streamline length.

A lofted surface, was generated from these smooth rings to create the interior surface of the inlet. This surface is shown in Figure 23. Once the interior surface was defined, the exterior of the surrogate model was then created.

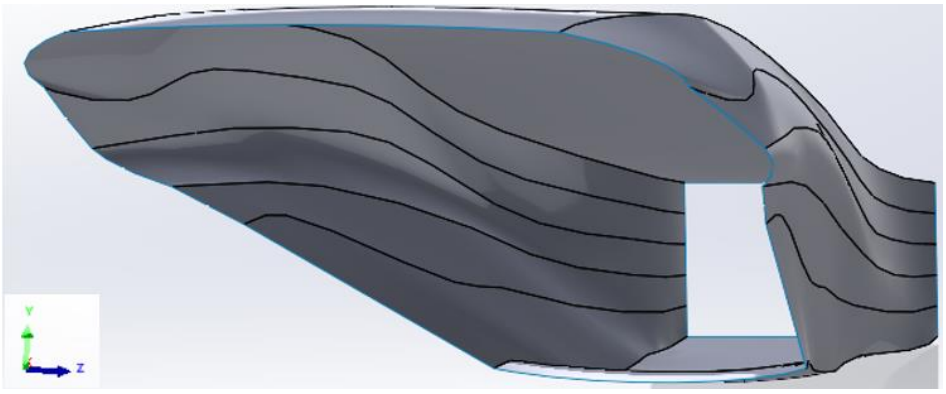

Figure 23: Lofted surface generated by the smooth rings. This surface will be used as the interior flow path surface.

The exterior surface started with the leading ring of the interior. That sketch was offset radially by $\frac{1}{100}$ of an inch to create a nominally sharp leading edge. This new offset sketch was then projected onto a plane parallel to the capture highlight and offset to create a 15-degree growth in all directions, resulting in a 15-degree beveled leading edge around the capture highlight of the inlet. A wireframe of this section is shown in Figure 24.

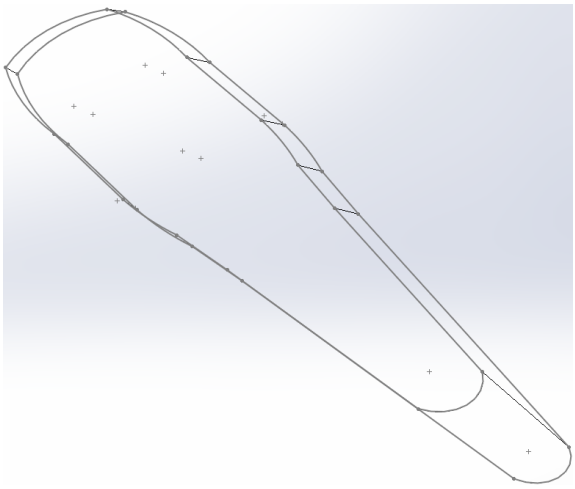

Figure 24: Isometric view of the two sketches used to generate the 15-degree beveled leading edge. This ensures a sharp edge, with an appropriate growth rate.

The section downstream of the sharp leading edge was produced by extending the rectangle at the isolator entrance downstream by three times the height in the streamwise direction (defining the length of the isolator). Using the interior surface and the leading edge, a simplified model was used in a CFD simulation, shown in Figure 25 to evaluate if the model would remain started, and has a similar shock structure to that of the HIFiRE-6 using the conditions from Table 2.

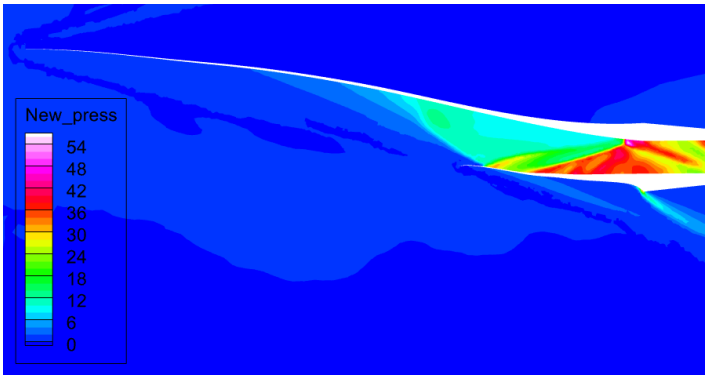

Figure 25: CFD Data collected of the interior surface and leading edge evaluated at the flight conditions used in previous testing [39]*. New_press is the pressure in psi, as the simulation produced Pa and needed to be converted. A lack of shockwave upstream of the cowl lip implies the model remains started.*

The outer mold line (OML) of the isolator section was defined by an offset of the interior surfaces three quarters of an inch below and to the sides, and the upper edge was extended to meet the vertical coordinate of the highest point of the leading-edge section. A lofted surface was created for the exterior between the OML of the isolator entrance and the downstream edge of the beveled leading-edge section. The solid model created from the CFD solution was scaled down by a factor of 3.64 to provide an isolator height of 0.5 inches. The resulting solid model is shown in Figure 26. This height was selected to maintain a total length that would fit within the confines of the reference test facility, while having an isolator section large enough to collect schlieren imagery.

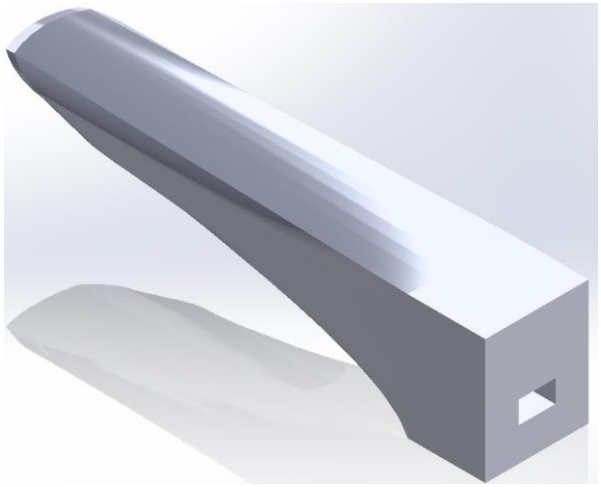

Figure 26: Isometric view of the solid model.

A model was built using additive manufacturing. An Open Additive™ PANDA™ machine was used to additively manufacture the model out of stainless-steel 316L. The PANDA™ machine is constrained to a total build height of 8.5 inches. To accommodate this constraint, the model had to be broken into two sections. The leading section was

digitally cut at eight inches to remain within the total length restriction of the additive manufacturing machine, while maintaining the leading edge of the inlet. However, the need to split the solid model introduced the need to connect the two parts. A lap joint with a cut into the leading section, and a matching extrusion on the trailing section was introduced to connect the two parts, Figure 27.

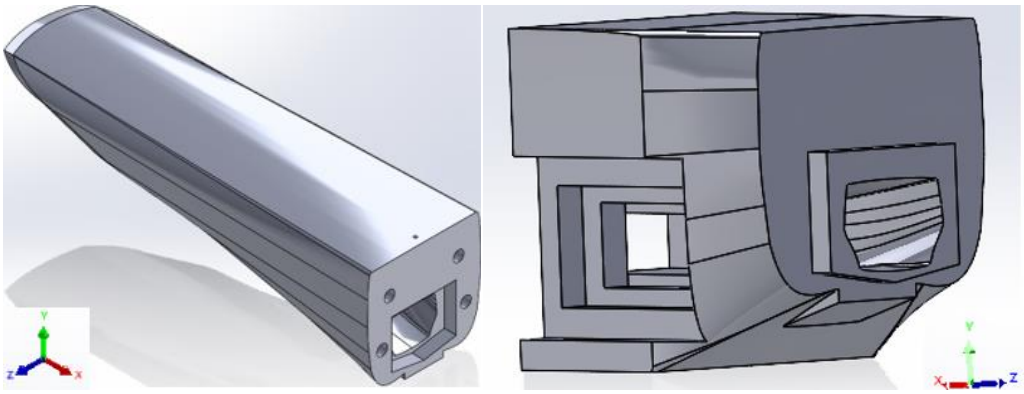

Figure 27: Views of the lap joint used to join the inner flow path of the model.

To accommodate schlieren imaging, a window was incorporated in the isolator section (Figure 28). Starting at the upstream edge on the inside of the isolator, a rectangular cutout of dimensions 0.7 by 1.5 inch was incorporated to allow the installation of a window. To avoid image distortion due to machining edges, the window was extended 1/10 of an inch in both vertical directions beyond the upper and lower surfaces of the isolator. A frame was then designed to hold the window in place while maintaining the curvature of the exterior.

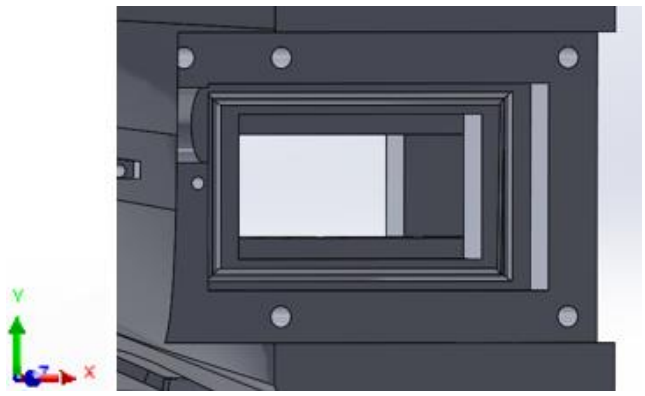

Figure 28: Side view showing the window to be used for schlieren imagery of the internal flow path. This window allows the visualization of the internal flow path in addition to pressure data.

Static pressure taps were also incorporated in the model to measure surface pressures along the IML. For each tap, 40/1000-inch ID holes were ‘drilled’ in the flow surface at the desired locations, Figure 29. 1/16-inch matched counterbored holes ‘drilled’ from the outer surface provided a means to install stainless-steel tubing with an outer diameter of 1/16-inch, and an inner diameter of 40/1000-inch to match the holes on the inner surface. This tubing is used to connect the pressure taps to a data acquisition system. A thickness of 1/16-inch separated the interior flow surface from the counterbore. The pressure ports are located along the upper and lower centerlines and along the sidewalls, with additional pressure taps at 45-degree radial locations at four stations in the streamwise direction. These four stations included an upstream location near the cowl lip, upstream of the separation bubble, the center of the bubble, and just downstream of the bubble as indicated in CFD. Because some of the pressure taps would be located on the windows, a metal blank was designed to replace the window and frame, with pressure taps installed therein. Trenches in the exterior surfaces of the model were provided for

routing of the tubing out of the model, while preserving the contours of the exterior surfaces.

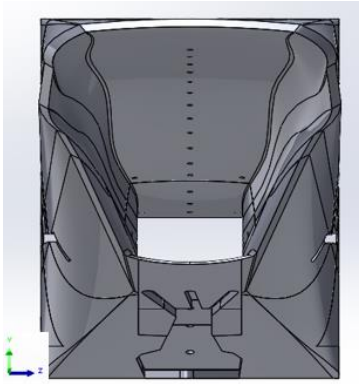

Figure 29: View from upstream of the inlet, showing the internal flow surface with visible pressure tap locations. Taps were along the upper and lower centerlines, the sidewalls, in addition to the corners where the separation bubble is located.

An existing wind tunnel strut was selected for use in mounting the model to the wind tunnel facility. A recessed plate was designed to interface between the model and strut. The completed model, including channels for routing instrumentation is given in Figure 30.

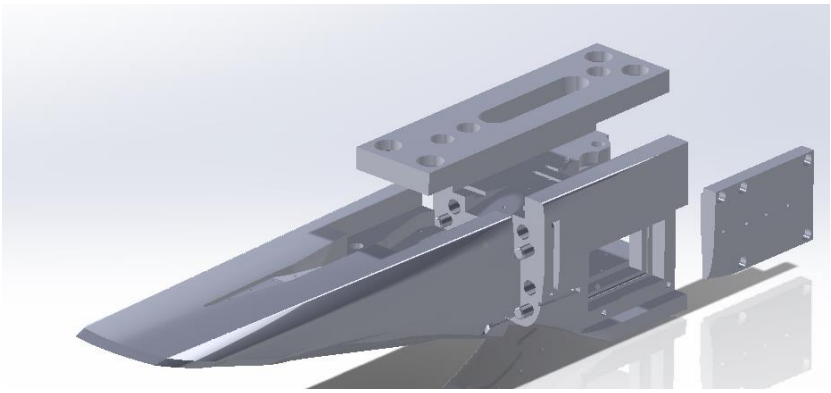

Figure 30: Exploded view of completed model, showing both sections after the break, instrument routing, the plate for mounting, and the blanks used for complete pressure data.

A flow chart of modeling the design process is shown in Figure 29, where decisions are shown with diamonds, looping back to where adjustments are applied.

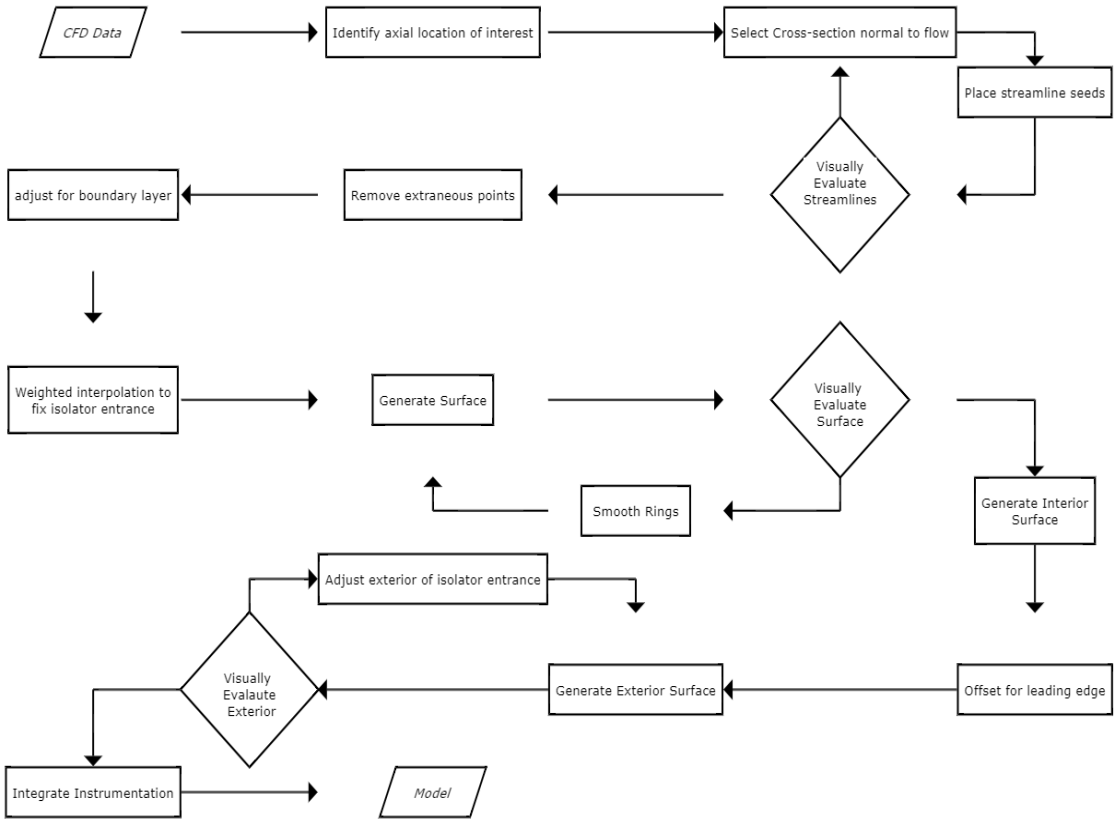

Figure 31: Flowchart of design process from CFD data to complete model, excluding integrating a lap-joint.

3.6 Structural Analysis

To determine the structural viability of the model (especially fasteners), a maximum load was estimated. The worst case was assumed to be a tunnel unstart condition, wherein a normal shock would develop on one half of the model, while free stream conditions existed on the other. Using normal shock relations and tunnel conditions, the maximum pressure load was calculated. Using this pressure and the maximum surface area, the stress across the fasteners was evaluated using the methods documented by Shigley [40] and determined to be within appropriate factors of safety. For surfaces, a safety factor of three was the minimum threshold, and 1.33 for fasteners. The lower threshold for fasteners was due to the fact that 75% of proof strength is used for pre-load for fasteners in tension. Finite Element Analysis was attempted, but grid generation using Hypermesh, the software available, had issues with the complex geometry of the model. SOLIDWORKS® was used assuming a thin surface thickness for preliminary analysis which resulted in meeting the desired factors of safety.

3.7 Manufacturing

An additive manufacturing approach was selected as an affordable means that would accommodate the complex nature of the relatively small inlet with inward turning geometry. The model was manufactured using an Open Additive™ PANDA™ Metal 3D Printing System, owned by Wright State University, using stainless steel 316L powder to laser weld the solid.

The amount of powdered Stainless Steel 316L that was needed for the print was determined by taking a volume of the six inch by six inch build area multiplied by the

total height of the build, eleven and a half inches. This was then multiplied by 0.7 to account for the compacting of the material during the weld process, and well as the density of 316L. Adding additional material for print failures, a total of 160 pounds of 316L powder was purchased. To provide an inert environment for the laser to weld without oxidation, dewars of nitrogen were needed.

CAD files of each component were uploaded into the PANDA™ system where a layer-by-layer grid (hatching) was generated. The hatch pattern used was stripes, which are alternating offset lines. Edges had a solid ring (contour), to improve surface roughness. The slice patterns are rotated 67 degrees after each layer, which are 40 microns thick . After printing, the material properties of the finished test article are more similar to welded metal rather than an extruded, machined part. The laser used to solidify the model causes the grain structure to be longer in the streamwise direction, due to the orientation of the hardware during the print. This length difference is caused by reheating, where the laser rewelds the two previous layers as it makes a new pass. A diagram provided by Open Additive™ illustrating the build process as well as hardware orientation is shown in Figure 32.

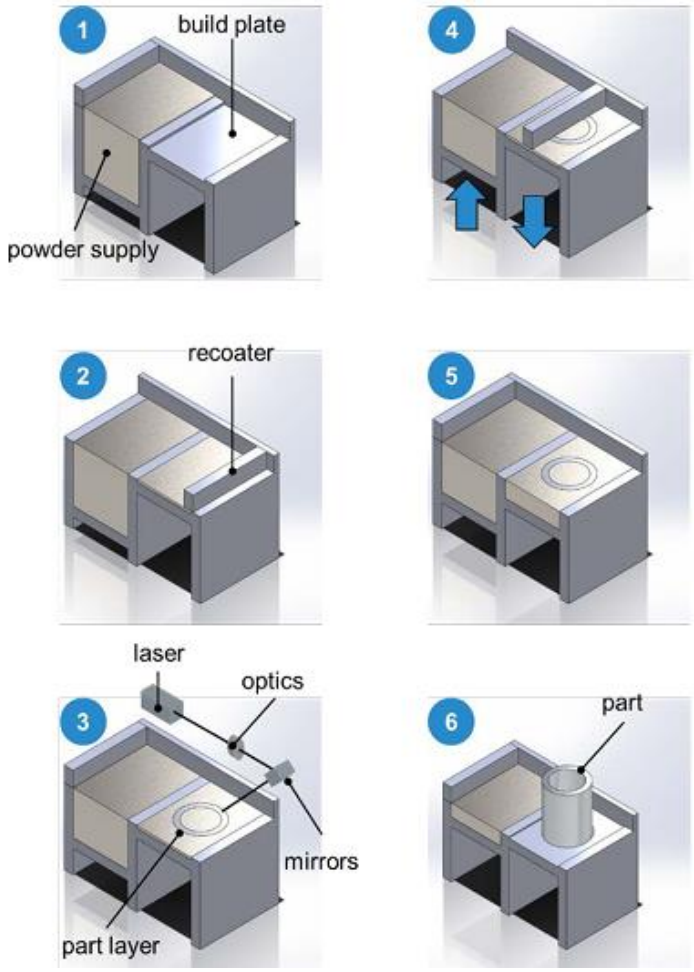

Figure 32: Open Additive™ PANDA™ additive manufacturing process and hardware configuration [41]. *Due to the size of the machine used, the model had to be split into sections.*

After a build is complete, the unused powder is removed from the build area and placed into a receptacle for cleaning and reuse. The entire machine is cleaned, save the supply section, using a shop vacuum to remove errant powder and soot followed by wiping everything down with isopropyl alcohol. The laser window is wiped down with isopropyl alcohol and methanol using laser wipes to not scratch the glass. The used powder is sifted through progressively finer mesh pans before being recycled into the powder supply.

A test section, the leading two inches of the model, was printed first. After a few hours of printing, the build failed. It was determined that the failure was because the geometry file generator had left an open space in the laser grid. This gap caused the laser weld to attempt to build on open space that caused loose slag to be generated. After the build area was cleaned, the file was repaired and the print restarted. A photograph of this test print is shown in Figure 33.

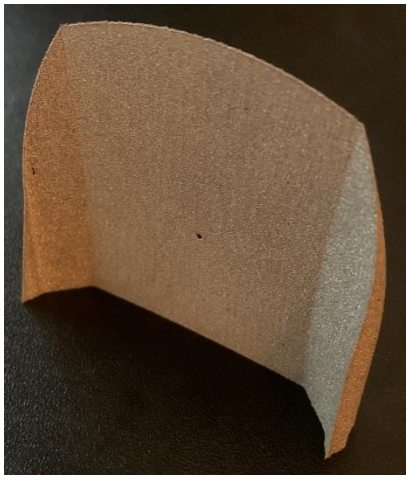

Figure 33: Test Print showing leading edge and a sample pressure tap

After completion, the test print was taken to GoHypersonic Inc. (GHI) to evaluate the surface roughness. The average roughness was found to 548 μin, which is roughly ten times rougher than acceptable. This indicated that post-processing would need to be done to ensure the model was ready for testing.

As the leading section is the longer of the two sections of the main model, it was printed first. However, modifications needed to be made to ensure printing would be successful. Supports were introduced to any surface parallel to the build plate. This is due to the laser weld being able to jump only a short distance without causing failure similar

to that of the test print. The first area needing support was the holes introduced to connect the recessed plate to the model. The supports used were 0.02-inch diameter posts perpendicular to the build plate with center distance of 0.03 apart, as shown in Figure 34.

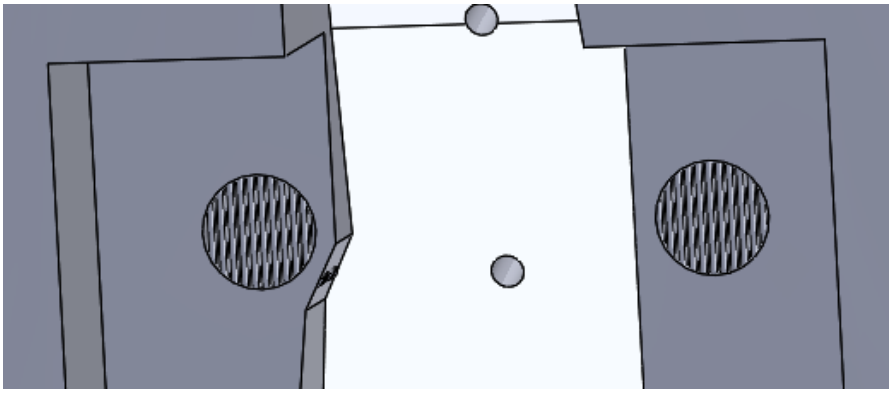

Figure 34: Section of the leading model section showing the supports added in the holes used to attach the model to the recessed plate.

The next area needing supports was the pressure tube routing originating from the sidewall pressure taps of the leading most ring. These supports, Figure 35, were the same geometry of the previous, but instead of being perpendicular to the build plate, they were extruded from the upper (leading) edge of the region and extruded at an angle. This meant that the supports only need to be removed from one edge, rather than multiple edges.

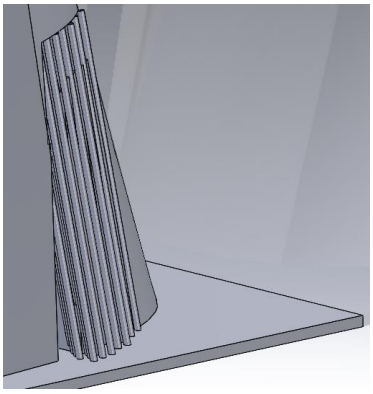

Figure 35: Supports applied to the routing from the leading most sidewall pressure taps, showing an angled support for ease of removal.

The final supports for the leading section, supported the edge of the space for the recessed plate shown in Figure 34. These supports, due to their length, were created as solid pieces that transitioned to the previously discussed posts. This difference was suggested by Open Additive after the first quarter inch of the print caused concern. Additionally, for all models after the test print, a raft of 0.02 inches was used for ease of removal of the model from the build, which will be discussed later. During this print the dewar of Nitrogen depleted and needed to be replaced. As the print was paused, and the build chamber filled with oxygen, a visible line was created where the print restarted due to oxidation. Open Additive suggested that this line was simply cosmetic. The final print, shown in Figure 36 shows the completed print. It can be observed that the surface finish of this model is much rougher than the test print. This is because taller, vertical prints have a tendency to show patterning more prominently.

Figure 36:Side (left),Top (center), Bottom (right) views of completed leading section of the model. Note supports from recessed plate edge, Discoloration line due to oxidation, and surface roughness of near vertical edge on body side(top)

After completion of the leading section, the trailing section was printed with the recessed plate. Similar supports were added to the model for each edge parallel to the build plate. To reduce the need for some supports, routing edges were changed to 40-degree slated edges or filleted. A drawing of these supports is given in Figure 37.

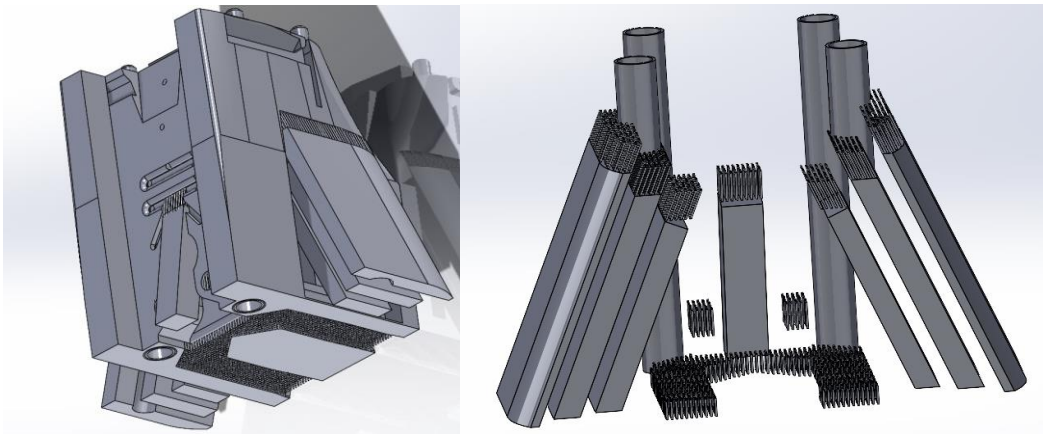

Figure 37: Views of the supports used to print the aft section of the model showing the supports with the main body (left), and the supports as stand-alone parts (right).

For this print, it was decided to treat the supports as a separate, stand-alone body to reduce print time as the laser pattern could be coarser for the supports.

In the last 0.3 inches of the print, another failure occurred. This was caused by a clogged air filter. When the filter clogged, the fan designed to maintain pressure began to run at an inappropriate level, this caused the powder in the build area to shift away from the part, causing concern. Initially, Open Additive believed that the issue was from a broken seal at the build plate. To remedy the perceived issue, the build with plate were removed, the seal replaced, and the plate reinstalled. However, when printing restarted, the fan issue was more apparent, allowing the real issue to be fixed. Unfortunately, during the reinstalling of the build plate, a slight shift occurred causing the print to be offset slightly. Figure 38 shows this offset, which caused the trailing edge section to be reprinted.

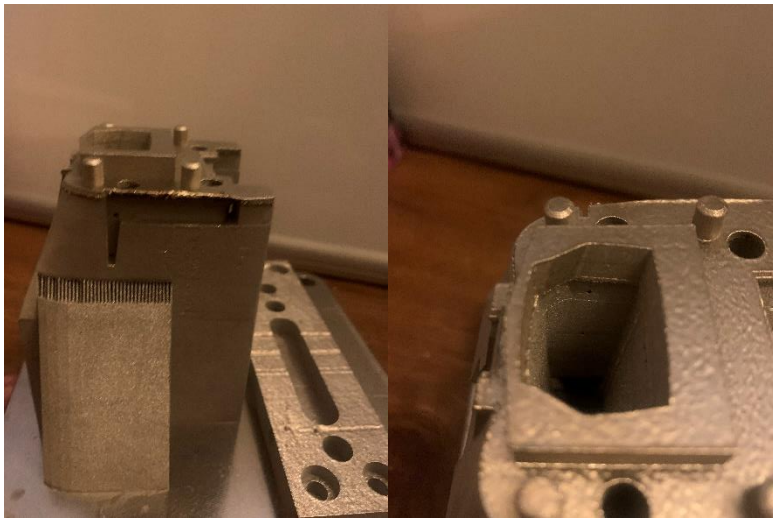

Figure 38: Images of print failure of trailing edge. (left) Exterior lip showing where powder moved away from part, (right) Interior showing step that required reprint.

The frames and blanks were produced in subsequent prints completing the manufacturing process.

3.8 Physical Model

The next step was to remove the manufactured pieces from their respective build plates. This was accomplished using a Wire EDM machine owned by Wright State University. This process was time consuming, because the loose powder between supports and in channels closed by the rafting material caused the wire to short frequently requiring restart. After all of the pieces were removed from the build plates, the supports were removed. The smaller posts were thin enough that a pair of mini pliers could be used to break each post close to the surface. The holes that were easily accessible were drilled out. Figure 39 and Figure 40 show the main body and peripherals of the model respectively.

Figure 39: Leading (left), Trailing (right) section of the main body of the model with supports removed.

The right of Figure 35 shows one of the supports for the counterbored holes used to connect the two sections of the model. Removing this support required a novel approach which will be discussed later. The blanks, used to collect pressure data in the windows,

also had the supports removed. The frames for the windows as well as the recessed plate did not need supports removed, as the counterbores were printed in such an orientation to remove the need for supports. These pieces are shown in Figure 40.

Figure 40: post-processed (left) window blank, (center) recessed plate, (right) window frame.

After the above-described post-processing was accomplished, an evaluation was performed to determine what post-processing work remained. It was determined that the use of a CNC mill would be the best approach to remove any excess material in the window spaces in the trailing edge, the recessed plate gap on the body side of both the trailing and leading sections, and the edges of the recessed plate, frames, and blanks. This would also clear the holes and slot of the recessed plate. Before this work was to take place the model was taken to the wind tunnel team at WPAFB for inspection and feedback. After examining the model, as it was, this team shared concerns about the work that would need to take place. The planned milling would not be an issue, but to smooth the surfaces even on the exterior around the window would take a great deal of hand work. It was decided that the only way using the methods available to the author would take weeks if not months. The need to mill the lap joint and pins placed at the lap joint to ensure a tight fit without hand grinding those areas was also pointed out. The wind tunnel

team was also extremely concerned about the surface roughness of the interior. As mentioned above, the length of the leading section of the model caused the surface finish to be rougher than that of the test section. It was suggested that an extremely thin layer of JB Weld (a high-temperature epoxy) could be applied to the surface to fill in the valleys of the print. The last application of epoxy could then be sanded smooth.

After consideration, the sponsors of this project, The Air Force Research Laboratory High Speed System Directorate Propulsion Branch, determined that these steps would require more time and effort than were available within the scope of this project. Therefore, the planned milling and other post-processing was not completed.

IV. CONCLUSIONS

4.1 Summary

To provide a fuller understanding of the flow physics along the interior flow path of a hypersonic inward turning compression system, such as that of the HIFiRE-6 configuration, a surrogate model was designed. With a rectangular isolator section visual measurement data, particularly schlieren imagery, can add additional data to the discrete pressure measurements that have been previously taken.

Streamline tracing using the CFD data from the HIFiRE-6 generated streamlines, through the use of a MATLAB script, were trimmed to only include the new surface. These new streamlines were adjusted to account for boundary layer thickness and smoothed to avoid abrupt steps. With these adjusted streamlines, an interior surface was generated. A solid model was then created, which was split into two sections due to manufacturing constraints. Windows were introduced to allow for schlieren imagery as well as pressure ports to collect pressure data.

A model was built using additive manufacturing facilities available to Wright State University. Challenges were encountered during the printing process and the physical model generated was deemed to require too much post-processing to make it suitable for wind tunnel testing. Therefore, the decision was made to have a new model manufactured using traditional machining methods by a contractor with experience in wind tunnel

model fabrication. This article will be used to perform the testing on the design. The test will not only evaluate the effects of the Shock Wave – Boundary Layer Interaction but also the viability of the model as a surrogate.

4.2 Future Work

Continuation of this work requires several more objectives to be completed. The first is the fabrication of the new model. It is suggested that the model be recreated in one solid piece, removing the lap joint and the bolts needed to hold them together. This would remove the issue produced by the supports of the counterbore, and any possibility that a joint will introduce unwanted disturbances into the inlet flow field.

Tools for analyzing the data will need to be created. Image reading scripts will need to be developed to take schlieren imagery and produce a data field to evaluate the shock structure as well as the extent and location of the separation bubble. This process can also be used to compare pressure data and CFD data to compare the surrogate to the HIFiRE-6.

The author also suggests that further work using the Open Additive PANDA machine be investigated to improve the surface finish of models generated, such that in the future the University may be able to produce its own models to be tested in a wind tunnel.

REFERENCES

[1] Fry, R. S. “A Century of Ramjet Propulsion Technology Evolution.” *Journal of Propulsion and Power*, Vol. 20, No. 1, 2004, pp. 27–58. https://doi.org/10.2514/1.9178.

[2] Segal, C. *The Scramjet Engine : Processes and Characteristics*. Cambridge University Press, Cambridge, 2009.

[3] Heiser, W. H., and Pratt, D. T. *Hypersonic Airbreathing Propulsion*. AIAA Education Series, Washington D.C., 1994.

[4] Faro, I. D. V. “Supersonic Inlets.” *AGARDograph-102*, May, 1965.

[5] Anderson, J. D. Modern Compressible Flow : With Historical Perspective. McGraw-Hill, Boston, 2004, pp. 86–97.

[6] Idris, A. C., Saad, M. R., Zare-Behtash, H., and Kontis, K. “Luminescent Measurement Systems for the Investigation of a Scramjet Inlet-Isolator.” *Sensors (Switzerland)*, Vol. 14, No. 4, 2014. https://doi.org/10.3390/s140406606.

[7] Weber, R. J., and MacKay, J. S. An Analysis of Ramjet Engines Using Supersonic Combustion. *Journal of Applied Physics*. Volume 14. http://link.aip.org/link/JAPIAU/v14/i8/p399/s1&Agg=doi.

[8] Flock, A. K., and Gülhan, A. “Viscous Effects and Truncation Effects in Axisymmetric Busemann Scramjet Intakes.” Vol. 54, No. 6, 2016. https://doi.org/10.2514/1.J054287.

[9] Billig, F. S. “SCRAM - A Supersonic Combustion Ramjet Missile.” *AIAA 93-2329*, 1993. https://doi.org/10.2514/6.1993-2329.

[10] Mölder, S., and Szpiro, E. J. “Busemann Inlet for Hypersonic Speeds.” *Journal of Spacecraft and Rockets*, Vol. 3, No. 8, 1966, pp. 1303–1304. https://doi.org/10.2514/3.28649.

[11] Taylor, G. I., and Maccoll, J. W. “The Air Pressure on a Cone Moving at High Speeds.” *Proceedings of The Royal Society A139*, Vol. 160, No. 62, 1932, pp. 278–297.

[12] Schlichting, H., Gersten, K., and Mayes, K. *Boundary-Layer Theory*. Springer Berlin Heidelberg, 2016.

[13] Van Wie, D. M., and Molder, S. “Applications of Busemann Inlet Designs for Flight at Hypersonic Speeds.” *Aerospace Design Conference, 1992*, 1992. https://doi.org/10.2514/6.1992-1210.

[14] Wie, D. M. Van. “Scramjet Inlets.” *AIAA Scramjet Propulsion*, 2001, pp. 447–511.

https://doi.org/10.2514/5.9781600866609.0447.0511.

[15] Yu, A., Yang, D., Yang, H., and He, J. “Experimental Research on Start Characteristics of a Hypersonic Inward- Turning Inlet.” *AIP Conference Proceedings 2027*, Vol. 030171, No. November, 2018. https://doi.org/10.1063/1.5065265.

[16] Moradian, N., Timofeev, E., and Tahir, R. “Theoretical Analysis of Self-Starting Busemann Intake Family.” *International Journal of Mechanical and Mechatronics Engineering*, Vol. 11, No. 5, 2017, pp. 933–942.

[17] Stephen, E. J., Hoenisch, S. R., Riggs, C. J., Waddel, M. L., McLaughlin, T., and Bolender, M. A. “HIFiRE 6 Unstart Conditions at Off-Design Mach Numbers.” *53rd AIAA Aerospace Sciences Meeting*, No. January, 2015. https://doi.org/10.2514/6.2015-0109.

[18] Dolvin, D. J. “Hypersonic International Flight Research and Experimentation (HIFiRE): Fundamental Sciences and Technology Development Strategy.” *15th AIAA International Space Planes and Hypersonic Systems and Technologies Conference*, No. May, 2008, pp. 1–11. https://doi.org/10.2514/6.2008-2581.

[19] Bowcutt, K., Paull, A., Dolvin, D., and Smart, M. “HIFiRE: An International Collaboration to Advance the Science and Technology of Hypersonic Flight.” *28th Congress of the International Council of the Aeronautical Sciences 2012, ICAS 2012*, Vol. 1, 2012, pp. 65–76.

[20] Bolender, M. A., Staines, J. T., and Dolvin, D. J. “HIFiRE 6: An Adaptive Flight Control Experiment.” *AIAA 2012-0252*, 2012. https://doi.org/10.2514/6.2012-252.

[21] Bisek, N. J. “High-Fidelity Simulations of the HIFiRE-6 Flow Path.” *54th AIAA Aerospace Sciences Meeting*, 2016. https://doi.org/10.2514/6.2016-1115.

[22] Sandham, N. D. “Shock-Wave / Boundary-Layer Interactions.” Vol. 1, pp. 1–18.

[23] Williams, S. *Three-Dimensional Separation of a Hypersonic Boundary Layer*. Imperial College of Science, Technology, and Medicine, London, 2004.

[24] Riley, N. “Shock Wave-Boundary-Layer Interactions, Edited by Holger Babinsky and John K. Harvey.” *Contemporary Physics*, Vol. 54, No. 1, 2013, pp. 62–63. https://doi.org/10.1080/00107514.2012.760652.

[25] Zhou, Y. Y., Zhao, Y. L., and Zhao, Y. X. “A Study on the Separation Length of Shock Wave/Turbulent Boundary Layer Interaction.” *International Journal of Aerospace Engineering*, Vol. 2019, 2019. https://doi.org/10.1155/2019/8323787.

[26] Anderson, B. H. *Design of Supersonic Inlets By a Computer Program Incorporating the Method of Chacteristics*. Washington D.C., 1969.

[27] Bricalli, M. G., Brown, L., Boyce, R. R., Gollan, R., Vanyai, T., and Pudsey, A. S. "Scramjet Performance with Nonuniform Flow and Swept Nozzles." *AIAA Journal*, Vol. 56, No. 10, 2018, pp. 3988–4003. https://doi.org/10.2514/1.J056963.

[28] Roberts, K. N., and Wilson, D. R. "Analysis and Design of a Hypersonic Scramjet Engine with a Transition Mach Number of 4.00." *47th AIAA Aerospace Sciences Meeting including the New Horizons Forum and Aerospace Exposition*, No. January 2009, 2009, pp. 0–29. https://doi.org/10.2514/6.2009-1255.

[29] Otto, S. E., Trefny, C. J., and Slater, J. W. "Inward-Turning Streamline-Traced Inlet Design Method for Low-Boom, Low-Drag Applications." 2015, pp. 1–18.

[30] Smart, M. K. "Design of Three-Dimensional Hypersonic Inlets with Rectangular-to-Elliptical Shape Transition." *Journal of Propulsion and Power*, Vol. 15, No. 3, 1999, pp. 408–416. https://doi.org/10.2514/2.5459.

[31] Slater, J. W. "Methodology for the Design of Streamline-Traced External-Compression Supersonic Inlets." *AIAA 2014-3593*, pp. 1–18. https://doi.org/https://doi.org/10.2514/6.2014-3593.

[32] Zare, M., Mousavi, S. M., and Nikjoo, A. M. A. H. "On the Application of Endoscopic Background-Oriented Schlieren Technique for Near-Field Investigation of Density Field." Vol. 13, No. 2, 2020, pp. 667–678. https://doi.org/10.29252/jafm.

[33] Settles, G. S. *Schlieren and Shadowgraph Techniques: Visualizing Phenomena in Transparent Media*. Springer US, New York, 2001.

[34] Regert, T., Grossir, G., and Blay, L. "Schlieren Visualization for High-Speed Flows Based on Laser-Induced Fluorescence." 2014. https://doi.org/10.1007/s00348-014-1668-x.

[35] Ã, M. J. H., and Settles, G. S. "A Comparison of Three Quantitative Schlieren Techniques." *Optics and Lasers in Engineering*, Vol. 50, No. 1, 2012, pp. 8–17. https://doi.org/10.1016/j.optlaseng.2011.05.012.

[36] Slater, J. W. "SUPIN : A Tool for the Aerodynamic Design and Analysis of Supersonic Inlets." No. 216, 2020, pp. 1–141.

[37] Busemann, A. "Die Achsensymmetrische Kegelige Uberschallströmung." *Luftfrahrtforschung*, Vol. 19, 1942, pp. 137–144.

[38] Anderson , J. D. *Hypersonic and High-Temperature Gas Dynamics*. AIAA Education Series, Reston, VA, 2019.

[39] Stevens, C. Personal Correpondance 12/12/2021.

[40] Budynas, R. G., and Nisbett, J. K. *Shigley's Mechanical Engineering Design*.

McGraw-Hill, New York, 2015.

[41] Open Additive. PANDA Build Configurations. https://openadditive.com/#panda. Accessed May 4, 2022.

APPENDIX A: SUPIN Input Data Explaining the Construction of an Input File

SUPIN is a tool developed by NASA GRC that uses defined conditions at different stations to generate a model geometry. The conditions are defined with input blocks, and passed through a Fortran program that outputs a point cloud for the geometry. Below is useful information in the construction of such an input file. Further detail is available in reference [36].

Station definitions

Freestream	0
Leading edge	L
End of external compression	EX
Downstream of normal Shock	NS
Cowl Lip	1
Throat	TH
end of internal compression	IN
Start of aft section of throat	TX
Start of the subsonic diffuser	SD
Engine Face	2

DATA BLOCK INFO

- Main input (ID 0)
  - Kmode 2
    - Design
  - Ktype 2
    - Two-dimensional, single duct
  - Kcomp 3
    - Supersonic flow through
  - Ksurf 1
    - Surface grids in plot3D
  - KgCFD 0
    - Do not generate CFD Grids
  - Kwinp 3
    - Specify Average engine face Mach
      - Station 2
  - Fwinp 2
    - We want Mach 2 at station 2
  - KWunit 0
    - Non-dimensional
  - Facap 0.5655
    - Reference capture area
  - Fwclip 0.3910
    - Aspect ratio at station 1
  - Wspillage 0
    - Flow ratio for spillage
  - Wbleed 0
    - Flow ratio for bleed
  - Wbypass 0
    - Flow ratio for bypass
  - Wother 0
    - Flow ratio for other

```
(blank spacer line)
-------------------------------------------------------------
DataID.  Main Control for SUPIN
  0
Kmode    Ktyp    Kcomp    Ksurf    KgCFD
  2        3        1        1        0
KWinp      FWinp      KWunit      FAcap      Fwclip
  3      0.520000        0      6.005044     1.0000
WRspill    WRbleed    WRbypass    WRother
0.02000    0.04000     0.00000    0.00000
```

- Free Stream (ID 1)
  - Kfs 6
    - Specify Reynolds/ft and Temp
  - Katm 0
    - Standard Model
  - Fsmach 6.0000
    - Freestream mach
  - Fsalpha 0
    - Angle of attack (can only be 0)
  - Fsbeta 0
    - Angle of sideslip (can only be 0)
  - Fsreyn 1.22E+07
    - Free stream Reynolds/ft
  - Fstemp 1000
    - Free stream temp (R)

Kfs	Katm	fsmach	fsalph	fsbeta
6	0	0.6000	0.000	0.000
fsreyn		fstemp		
2.5E+06		390.0		

- Approach flow(ID 2) (defaults to happen)
  - Kapp 0
    - No approach flow
  - I think the rest can be neglected
- External Supersonic Diffuser (ID 4)
  - Kexd 4
    - Three stage ramp
      - Second stage isentropic may not be needed, could lengthen
  - fptEXptL
    - Total pressure between L and EX
  - Fpt1ptex
    - Total pressure ratio between EX and 1
      - Positive is us defining, negative allows SUPIN to decide

```
DataID.  External Supersonic Diffuser
  4
Kexd     FptEXptL     Fpt1ptEX
 ##       -0.9950      -0.9850
        :
  Additional input lines defined according to Kexd
        :
```

- Cowl lip (ID 5)
  - ARclin 1
    - Aspect ratio of major to minor axis of cowl lip ellipse
  - Fbclin 0.0001
    - Length of minor axis (needs to be this sharp for supersonic)
  - Fthclin 27
    - angle of cowl lip interior (deg)
  - ARclex
    - aspect ratio for exterior
  - Fbclex
    - Length of minor axis of exterior
  - Fthclex
    - Angle of exterior

```
DataID.  Cowl Lip Profile
  5
ARclin    Fbclin    Fthclin     ARclex    Fbclex    Fthclex
 2.000    0.00200    10.000      2.000    0.00200    15.000
```

- Cowl exterior
  - Kcwex 0
    - No cowl lip exterior is created
  - The rest should be neglected

```
DataID.  Cowl Exterior
  6
Kcwex     Frcwex     Fxcwex     thswex
  1       1.1500     -2.000      5.000
```

- Throat Section (ID 8) forward part of internal ducting
  - Kthrt 5
    - Planar 2D inlets
  - fptTHpt1
    - Ratio of total pressures between 1 and TH
  - fptTXptTH
    - ratio of total pressures between TH and TX

- fptSDptTX
  - ratio of total pressures between TX and SD

```
DataID.  Throat Section.
  8
Kthrt    FptTHpt1    FptTXptTH    FptSDptTX
 ##      -0.99000     -0.99500     -1.00000
        :
  Additional input lines defined according to Kthrt
        :
```

- Subsonic Diffuser (Will be treated as isolator due to supersonic flow through) (ID 10)
  - Ksubd 4
    - 2D single duct
  - Klsubd 1
    - Specify the length
  - FLsubd
    - That length
  - Theqsd 7
    - Equivalent conical angle (deg)
  - Fpt2ptSD
    - Total pressure ratio within subsonic diffuser

```
DataID.  Subsonic Diffuser
 10
Ksubd     KLsubd     FLsubd     theqsd     Fpt2ptSD
  2          1      4.50000      3.000     -0.97500
        :
  Additional input lines defined according to Ksubd
        :
```

- Engine Face (Rear of isolator) (ID 11)
  - Kxef 2
    - Engine is placed at end of isolator
  - Fxef
    - location
  - kyef 6
    - Engine face is centered with isolator
  - Fyef
    - Location
  - Thetef 0
    - Angle from normal
  - Kef 1
    - Circular with no spinner

```
DataID.  Engine Face
 11
KxEF      FxEF      KyEF      FyEF      thetEF
  2     6.00000       1     1.00000      0.000
KEF
 1
 diamEF
 3.00000
```

APPENDIX B: Sample SUPIN Input File Used to Generate a Model Geometry

SUPIN: 2D Supersonic Outflow Inlet.

High-Speed Inlet. Mach 6.0.

HIfiRE 6 three stage

DataID. Main Control for SUPIN

0

Kmode Ktyp Kcomp Ksurf KgCFD

2 2 3 1 0

KWinp FWinp KWunit FAcap Fwclip

3 4.0000 0 10.000000 4.000

WRspill WRbleed WRbypass WRother

0.01000 0.00000 0.00000 0.00000

DataID. Freestream

1

Kfs Katm fsmach fsalph fsbeta

6 0 6.000 0.000 0.000

fsreyn fstemp

1.22E+07 1000

DataID. External Supersonic Diffuser

4

Kexd FptEXptL Fpt1ptEX

7 -0.9950 -0.9850

Nstgs thstg1 thstg2 Kmtexd Fmtexd

3 8.000 7.50 1 4.200

Knose Frnose

1 0.05000

DataID. Cowl Lip

5

ARclin bclin thclin ARclex bclex thclex

2.000 0.0002 7.000 2.000 0.0002 -5.000

DataID. Cowl Exterior

6

Kcex Frcex Fxcwex thswex

1 1.1500 30.000 5.000

DataID. Throat

8

Kthrt FptTHpt1 FptTXptTH FptSDptTX

6 -0.99000 -0.96000 -0.96000

Fdxcbsh Fdycbsh FLshTX FLTXSD

1.5000 0.0000 4.0000 2.0000

thcbTX FmachTX FaSDaTX Fcwds Fcbds

-5.000 3.0000 1.0200 0.300 0.100

DataID. Subsonic Diffuser

10

Ksubd KLsubd FLsubd theqsd Fpt2ptSD

4 2 15.0000 2.000 -0.97500

FNcwSD FNcwX FLcwX Ksdprp Ksdvar

0.3300 0.2000 0.1000 0 0

DataID. Engine Face

11

KxEF FxEF KyEF FyEF thetEF

2 1.00000 6 1.00000 0.000

KEF

1

diamEF

2.50000

DataID. Grid Spacing

13

Fgdds Rgsmax Fdswall Fdssym Fdscex Fdsthrt

1.000 1.15 0.000010 0.00500 0.00500 0.00500

Ddinf Ddfar Ddnoz Ddclp thfar Fgnoz

0.0500 5.000 2.000 0.0040 25.000 0.0950

DataID. Summary Table

99

Ktab1

1